Applied Catalysis B: Environmental 219 (2017) 672–682

Contents lists available at ScienceDirect

Applied Catalysis B: Environmental

journal homepage: www.elsevier.com/locate/apcatb

Research Paper

Exploration of the mechanism of chemical looping steam methane reforming using double perovskite-type oxides $La_{1.6}Sr_{0.4}FeCoO_6$

Kun Zhao[a,b,c,d], Anqing Zheng[a,b,c], Haibin Li[a,b,c], Fang He[a,b,c,*], Zhen Huang[a,b,c], Guoqiang Wei[a,b,c], Yang Shen[d], Zengli Zhao[a,b,c]

[a] Guangzhou Institute of Energy Conversion, Chinese Academy of Sciences, China
[b] CAS Key Laboratory of Renewable Energy, China
[c] Guangdong Provincial Key Laboratory of New and Renewable Energy Research and Development, China
[d] University of Chinese Academy of Sciences, Beijing 100049, China

ARTICLE INFO

Article history:
Received 13 June 2017
Received in revised form 28 July 2017
Accepted 7 August 2017
Available online 8 August 2017

Keywords:
CL-SMR
Double perovskite
Mechanism
Reaction boundary
Synergistic effect

ABSTRACT

Co-production of syngas and hydrogen via chemical looping steam methane reforming (CL-SMR) using double perovskite-type oxide $La_{1.6}Sr_{0.4}FeCoO_6$ as an oxygen carrier was studied. The reaction mechanisms, including the synergistic effects, the metal transitions, the oxygen diffusion and the migration of reaction boundary during the two-step reactions, were systematically investigated by the characterizations of the oxygen carriers at different reaction stages using XRD, XPS, H_2-TPR and TG technologies. Meanwhile, isothermal reactions were carried out in a fixed-bed reactor to analysis the reaction products. Three reaction stages including the total oxidation of methane with the active adsorbed oxygen, partial oxidation of methane with the lattice oxygen, and the methane decomposition were identified, using the surface of the oxygen carrier particles as reaction boundary. A large number of syngas was generated due to the concordant of methane dissociation with the lattice oxygen diffusion, and the resistant to coke formation was enhanced effectively. In the steam dissociation stage, the deep reduced metals (Fe^{2+} and Co^0) combining with the abundant oxygen vacancies provided enough active sites for the breakage of H—O bond of H_2O. The oxygen vacancies were neutralized immediately by the O atom, and the two H atoms combined together to form amounts of H_2. These results suggested that, the positive roles displayed by the synergistic effects between multi-metals in double perovskite structure could effectively promote the partial oxidation of methane and steam splitting. It provides a potential way to develop more active oxygen carrier for CL-SMR to co-produce syngas and hydrogen by comprehensively considering the methane dissociation and the lattice oxygen diffusion.

© 2017 Elsevier B.V. All rights reserved.

1. Introduction

As a competitive fuel with "3A" features of abundant, affordable and acceptable, natural gas is receiving more and more attentions for its conversion and utilization. Generally, the key component of natural gas is methane, accounted for more than 90% of contents. Therefore, the conversion and utilization of natural gas is mainly concentrated on the exploration of methane, which is firstly converted to syngas, then to be used for Fischer-Tropsch synthesis or as feedstock for the synthesis of some other chemicals. The preparation of the intermediate product of syngas is prioritized for researches. Currently, the most common and typical method for syngas production is the technology of partial oxidation of methane (POM) [1–3]. In POM process, precious metals such as Pt and Pd exhibit good reactivity and anti-carbon capacity. But the expensive prices of precious metals dragged down the industrialized applications. Another been largest used catalysts of Ni-based oxides, brought about serious carbon deposition and catalysts deactivation. Besides, the existence of gaseous oxygen in the POM reaction is easily to cause total oxidation of methane to generate CO_2 and H_2O, and the risk of explosion owing to the premixing of CH_4/O_2 is also existed. On the other hand, as a clean, efficient and sustainable new energy with the most development potential, hydrogen is widely used in petrochemical, clean coal, fuel cell and some other aspects. The enormous demands for hydrogen greatly motivate the technology of hydrogen production. Steam methane reforming (SMR) is a mature technology for methane conversion to produce

* Corresponding author at: Guangzhou Institute of Energy Conversion, Chinese Academy of Sciences, China.
E-mail address: hefang@ms.giec.ac.cn (F. He).

http://dx.doi.org/10.1016/j.apcatb.2017.08.027
0926-3373/© 2017 Elsevier B.V. All rights reserved.

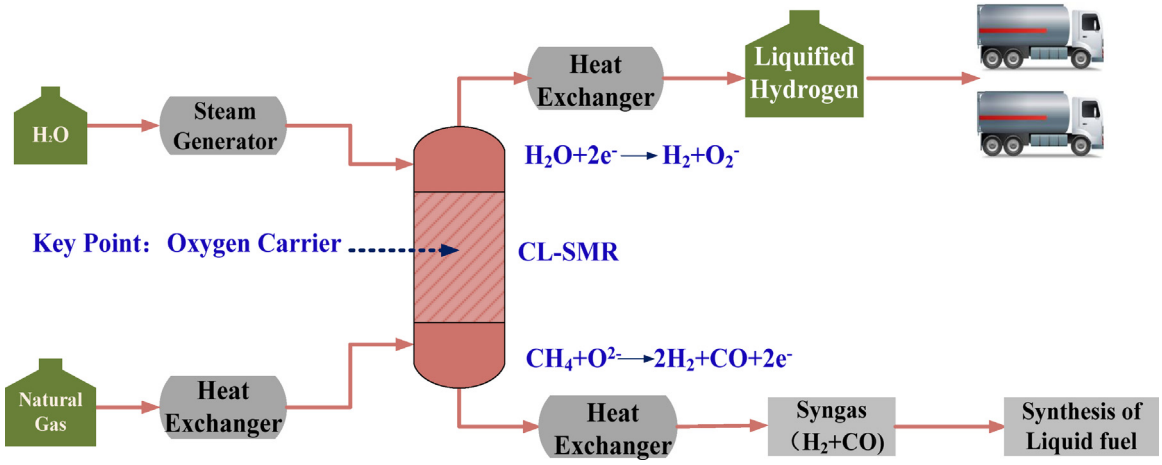

Fig. 1. Process flow sheet of CL-SMR.

hydrogen-rich syngas ($CH_4 + H_2O \rightarrow CO + 3H_2$) [4–6], which need an additional water-gas shift reaction to obtain pure hydrogen, and consequently leading to the high costs and energy penalty. Based on the urgently requirements for methane conversion, as well as syngas and pure hydrogen production, a novel technology of chemical looping steam methane reforming (CL-SMR) is causing researchers' attentions, due to its energy-efficient and low-cost route. In the CL-SMR process, methane is partially oxidized to syngas by the lattice oxygen of the oxygen carrier in the reforming reactor, and then the reduced oxygen carrier is regenerated by steam to recover oxygen and simultaneously to produce hydrogen due to the steam dissociation. Usually, an air oxidation stage is also needed if the oxygen carrier cannot be completely regenerated by steam [7]. The process flow sheet of CL-SMR is shown in Fig. 1, the product syngas can be used as feedstock to be converted to liquid fuels or other chemicals, while the product hydrogen from the second step can be directly utilized for fuel cells or for some other aspects. This concept was first proposed by Steinfeld et al. [8,9] who combined the methane reforming with metal-oxide reduction for the high-temperature solar chemical process. At 2003, Kodama et al. [10] tested the two-step cyclic steam reforming of methane by using WO_3/ZrO_2 as catalyst to produce CO-rich syngas and hydrogen, which was also the same process as CL-SMR. They predicted that the produced syngas had the H_2/CO ratios of about two, which was suitable for methanol production. By means of the capacity for oxygen delivery, the oxygen carrier plays the most important role in the CL-SMR process for oxygen transfer and heat-carrying, consequently to make the full use of the hydrocarbon resource for the co-production of syngas and hydrogen. Therefore, the key point of the implementation of CL-SMR is to choose the optimal oxygen carrier with high syngas selectivity, excellent resistance to carbon formation, good thermo stability and superior steam splitting capacity.

Perovskite-type oxide is a recently springing-up catalyst due to its good activity and high thermal stability, with a general formula of ABO_3, where A site is occupied by a rare earth metal or/and alkaline earth metal and B-site is a transition metal. In the perovskite structure, metal in A-site is coordinated with six oxygen atoms, while metal in B-site is coordinated with twelve oxygen atoms. Different from other mixed oxides [11–14], perovskite-type oxide can serve not only as lattice oxygen carrier but also as catalyst for CH_4 activation due to its special structure [15]. Hence it provides a good potential for oxygen supply and exhibits good activity through the cooperation of multi-metals. Among various perovskite-type oxides, $LaFeO_3$ is the most extensively used due to its good capacity for oxygen delivery [16,17]. Dai et al. [18,19] prepared perovskite $LaFeO_3$ for partial oxidation of methane and found that it exhibited high catalytic activity and good selectivity towards CO and H_2. Mihai et al. [20] reported that the crystal size of $LaFeO_3$ played a significant role in determining the catalytic properties for the partial oxidation of methane. Larger crystal size could lead to lower Fe—O bond energy, and consequently produce syngas with higher selectivity. Zheng [21] reported macroporous $LaFeO_3$ supported CeO_2 as oxygen carrier for chemical-looping reforming of methane. The presence of CeO_2 on $LaFeO_3$ improved the reducibility, oxygen mobility and reactivity for methane oxidation due to the coexistence of Ce^{3+} and Fe^{2+} irons. Based on these, various perovskites with partial substitution of metals were further investigated. He et al. [22] prepared $La_{1-x}Sr_xFeO_3$ with partial substitution of La^{3+} by Sr^{2+} and demonstrated its improvement on the reactivity due to the generation of more oxygen vacancies. Taylor et al. [23] reported the $La_{1-x}Sr_xFeO_{3-\delta}$ as an oxygen storage material in methane reforming reaction and demonstrated its high selectivity, fast oxide diffusion, and redox stability. Evdou et al. [24] prepared $La_{1-x}Sr_xFeO_{3-\delta}$ for simultaneous production of synthesis gas and pure hydrogen in a dense mixed conducting membrane reactor. They found that the addition of small quantities of NiO in the perovskites could effectively increase the reactivity of methane decomposition, selectivity of syngas and capacity for water splitting. Li et al. [25,26] investigated $La_{0.8}Sr_{0.2}FeO_3$ (LSF) and LSF supported core-shell Fe_2O_3@LSF for partial oxidation of methane. The high activity of oxygen carrier is largely attributed to the enhanced O^{2-} and the electron transports facilitated by the LSF support. The above researches showed that, the metals in A site were non-catalytic; they had effects on the amounts of oxygen vacancies and the valence states of metals in B site, and consequently indirectly affect the reactivity. While as the dominating active component, the metals in B-site play a direct role on the improvement of reactivity due to the synergistic effects between metals. Galinsky [27] investigated the effects of various B-site dopants of Al, V, Fe, Co and Ni for $CaMnO_3$ based oxygen carrier and found that $CaMn_{1-x}Fe_xO_{3-\delta}$ have the best redox activity in 100 redox cycles. Nalbandian et al. [28] investigated $La_{1-x}Sr_xM_yFe_{1-y}O_{3-\delta}$ (M = Ni, Co, Cr and Cu) as oxygen carrier for chemical looping methane reforming. By ranking the performances of all the oxides from the points of syngas yields as well as the oxygen that can be delivered to fuel, the sample $La_{0.7}Sr_{0.3}Cr_{0.1}Fe_{0.9}O_3$ mixed with 5% NiO exhibited the best reactivity with 90% yield of H_2. Zhao et al. [29] prepared perovskites $LaFe_{1-x}Co_xO_3$ (x = 0.1, 0.3, 0.5, 0.7, 1.0) for chemical looping steam methane reforming and found that the suitable substitution value of Co ion in B-site could obviously improve the reactivity and inhibit CH_4 decomposition. The increased oxygen vacancies on the $LaFe_{0.7}Co_{0.3}O_3$ could counteract the negative effect of material sintering.

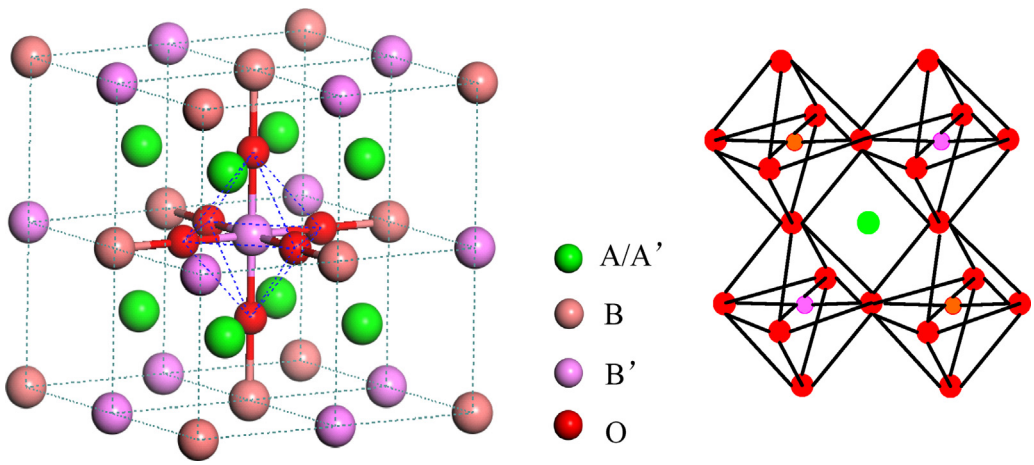

Fig. 2. Typical structure of double perovskite-type oxide.

Derived from the perovskite-type oxides, double perovskite-type oxide (DPO) with formula of AA'BB'O_6 is another attractive oxygen carrier due to its unique structure and property. In the double perovskite structure, octahedron B-O_6 and B'-O_6 are alternatively arranged by using a corporate apical angle, while the A and A' metals are filling in the center of four octahedrons, as shown in Fig. 2. Similarly to the single perovskite-type oxide, DPO is also a material which obtained after calcination at high temperature. Therefore, a stable skeleton structure can be formed to possess excellent thermo stability. But superior to others, the structure of DPO is orderly arranged with unique octahedron and its catalytic performance has a more promising potential for improvement. The coordinated B-O-B' combinations with different ionic radius and different exchange interactions, playing important roles for the increase of oxygen defects and enhancement for the oxygen transport. Besides, the multi-metals in DPO structure can provide expansive combination spaces for researchers and the synergistic effects between multi-metals can be presented more remarkable to change the reactivity. Initially, DPOs are widely used as superconducting materials and magnetic materials due to their efficient and stable properties [30–33]. Then it was firstly been used for methane combustion by Falcón [34] at 2004, who prepared DPOs $A_2FeMoO_{6-\delta}$ (A = Ca, Sr and Ba) and made them possible catalysts. After that, more and more researches on the catalytic properties of DPOs began to appear. Li et al. [35,36] used $Sr_2Mg_{1-x}Fe_xMoO_{6-\delta}$ and $Sr_2Mg_{1-x}Mn_xMoO_{6-\delta}$ as catalysts for methane oxidation and found that the catalytic property of DPO was strongly influenced by the substitution of metal in B-site and the enhancement reactivity was correlated with the lattice oxygen species on the Fe/Mn-relating surface. Hu and his co-works [37–39] prepared DPOs such as La_2CuNiO_6, La_2CoMnO_6/CeO_2 La_2NiAlO_6, etc. as catalysts for methane combustion. The DPOs exhibited more excellent performances than single perovskite-type oxide due to their unique structures, distinct surface properties, and the strong intergrowth interactions between multi-metals. Tuza [40] prepared La_2NiTiO_6 for steam reforming of methane. An improved reactivity was achieved to produce syngas with H_2/CO molar ratio of 3.0, which was ascribing to the increased active sites and/or metal-support interactions. The researches above indicated that DPOs may create a promising feasibility as catalysts for methane conversion. But presently, the report about using DPO as oxygen carrier for CL-SMR is rarely seen, which may be due to the challenges of uncertainty and complexity of the unique structure of DPO. In our previous investigation [41], we established the DPOs $La_{1-x}Sr_xFeCoO_6$ (x = 0, 0.2, 0.4, 0.6, 0.8, 1.0) as oxygen carriers and demonstrated the feasibility of them for CL-SMR to co-produce syngas and hydrogen. Among them, $La_{0.6}Sr_{0.4}FeCoO_6$ exhibited the best oxygen transport ability, thermal stability, as well as capacity for hydrogen generation. But the details and the mechanism of the reactions do not studied thoroughly. Herein, we use $La_{0.6}Sr_{0.4}FeCoO_6$ as oxygen carrier for CL-SMR, and focus on discussing the synergistic effect, the metal transition, the oxygen delivery and the product generation systematically. Finally, the mechanism of the reactions including the pathways of methane reduction and steam dissociation for CL-SMR over double perovskite-type oxide is proposed.

2. Experiment

2.1. Synthesis of the DPO $La_{1.6}Sr_{0.4}FeCoO_6$

Micro-emulsion method was used to prepare the DPO $La_{1.6}Sr_{0.4}FeCoO_6$. The required amounts of $La(NO_3)_3{\cdot}6H_2O$, N_2O_6Sr, $CoN_2O_6{\cdot}6H_2O$ and $Fe(NO_3)_3{\cdot}9H_2O$ were weighed at a desired stoichiometric ratio and dissolved in deionized water. Then the surfactant Tritonx-100, cosurfactant n-butyl alcohol and oil phase cyclohexane were added to make a mixture of solution A. Meanwhile, the same ratio of surfactant Tritonx-100, cosurfactant n-butyl alcohol and oil phase cyclohexane were added into $(NH_4)_2CO_3$-NH_4OH to make a mixture of solution B. After that, the solution B was slowly dripped into solution A to form sediment under a water bath at 50 °C. The sediment was allowed to settle for 2 h and filtered. Then the sediment was dried overnight in a convection oven at 110 °C. Finally, the as-prepared precursor was thermally decomposed at 500 °C for 2 h and calcined at 1000 °C for 6 h.

2.2. Characterization

X-ray diffraction (XRD) and X-ray photoelectron spectroscopy (XPS) technologies were adopted to characterize the oxygen carriers at different reaction stages to master the physical and chemical changes during the two-step reactions. The oxygen carriers at different reaction stages were rapidly cooled down in N_2 atmosphere and taken out at room temperature, and then to be characterized. The crystal phases of the oxides were identified by XRD in a Japan Science D/max-R diffractometer with Cu Kαradiation (λ = 0.15406 nm), operating voltage of 40 kV and current of 40 mA, and the diffraction angle (2θ) was scanned from 10° to 80°. As a powerful tool to study the surface properties of material, XPS technology is sensitive to the chemical environment and can give information about the oxidation state of the surface elements. XPS was used to probe the near-surface composition of the oxides. The

equipment was Thermo Fisher Scientific Inc with an Al Kα X-ray source at an operating voltage of 20 kV and a current of 10 mA, under the conditions of 20 eV and 100 eV pass energy for the survey spectra and the single element spectra. The hydrogen-temperature programmed reduction (H_2-TPR) experiment was used to test the reducibility of oxygen carrier, which was conducted in 5.0 vol% H_2 balanced with helium at a flow rate of 60 ml/min from room temperature to 1000 °C with a heating rate of 10 °C/min, and then stayed at 1000 °C for 30 min. Thermo-gravimetric analyzer (NETZSCH STA409C/PC) was used to investigate the reactivity of oxygen carrier with methane. In each test, about 20 mg oxygen carrier were heated in an alumina crucible from 30 °C to 850 °C with a heating rate of 20 K/min with argon stream as purge gas. When the temperature rose to 850 °C, the CH_4 stream (5.0 vol% CH_4 + 95% vol% N_2) was introduced in and the weight loss was recorded automatically.

2.3. Reactivity test

The fixed-bed reactor was a quartz tube with a baffle in the middle part that only allows gas to get through. 2.0 g of the oxides (particle size 80–100 mesh) were placed on the baffle under atmospheric pressure at 850 °C to react with methane and then with steam. The product gases out of the reactor were collected with gas bags and analyzed by a gas chromatograph (Shimadzu GC-2010 plus). The detailed process of the reaction was introduced in the previous research [42].

3. Results and discussions

3.1. XRD analysis in methane reduction step

The XRD patterns of $La_{1.6}Sr_{0.4}FeCoO_6$ at different reduction stages, which is reacting with methane for 3 min, 6 min, 9 min, 12 min, 15 min, 18 min and 20 min, are shown in Fig. 3. It can be seen that, the XRD pattern of the fresh $La_{1.6}Sr_{0.4}FeCoO_6$ obtains the desired double perovskite crystal form which is in agreeement with Joint Committee on Powder Diffraction Standards (JCPDS) card of $La_{1-x}Sr_xFeCoO_z$. Besides, the characteristic peaks of $SrCoO_z$ at $2\theta = 28.625°$ and 32.019° are also observed, ascribing to the antisite defects from the ideal double perovskite crystal structure which are aroused by the coordination disorder of multi-metals. Antisite defect in the double perovskite structure is inevitable, but may play a vital role for the physical properties [43]. After react with methane from 3 min to 6 min, the characteristic peaks of double perovskite structure are still maintained, but come with some impurity phase representing the emerge of Fe_2O_3 and CoO. The metals Fe and Co in B and B' sites separate out from the double perovskite structure immediately in the reducing atmosphere. When the reaction proceeds to 9 min, the characteristic peaks of Fe_3O_4 are emerged to replace that of the Fe_2O_3, ascribing to the reduction of Fe^{3+} to Fe^{2+}. Besides, the characteristic peaks of Co^0 are emerged obviously at this moment, due to the deep reduction of Co^{2+} to Co^0. The active metal Co is easily to be reduced to single-metal. Then as the reaction proceeds, the new oxide of La_2SrO_x is detected at 12 min and its characteristic peaks gradually increase until 18 min. During this stage, the double perovskite structure gradually recede, corresponding to the enhancement of SrO and CoO with the characteristic peaks at $2\theta = 27.25°$, 31.566°, 45.234°, 49.613° and $2\theta = 36.617°$, 42.347°, 42.883°. Meanwhile, Fe_3O_4 is further reduced to FeO. When the reaction proceeds to more than 18 min, it can be obviously seen that the characteristic peaks of double perovskite structure and $SrCoO_z$ are almost disappeared. The sample at this state is primarily existed in the forms of La_2SrO_x with some other kinds of oxides such as La_2O_3, SrO, CoO, Fe_3O_4, FeO and Co^0, indicating the stepwise reduction of high valence states of Fe^{4+}/Fe^{5+} to Fe^{3+} and to Fe^{2+}, combining with the reduction of Co^{3+} to Co^{2+} and then to Co^0. While the La^{3+} and Sr^{2+} in A and A' sites maintain their valence states and appear in the form of La_2O_3 and SrO.

3.2. XPS analysis in methane reduction step

The chemical states of surface metals of La3d, Sr3d, Fe2p and Co2p on the samples at different reduction stages are investigated by fitting the XPS curves as shown in Fig. 4. In Fig. 4a, two doublets peaks namely $La3d_{3/2}$ and $La3d_{5/2}$ with two additional splitting peaks are existed in the XPS spectra of La3d, which are similar with the form of the standard trivalent La3d spectrum. It means that the metal La in $La_{1.6}Sr_{0.4}FeCoO_6$ is existed in the form of the typical compounds of La^{3+}. The peak shapes and peak areas of the samples at different reduction stages exhibit no obvious change, strongly indicating that the cation La in A-site does not take part in the reduction reaction. But the metal La may exist in a different coordination environment, attributing to the formation of new species such as La_2SrO_x and La_2O_3 which are detected by XRD. The different coordination environment also relates to the shifting of the binding energy (E_B) of the main peak $La3d_{5/2}$, which shifts slightly to the higher E_B value, suggesting the lower covalence of La—O bond, which consequently representing the reduce of the structure stability as the reaction proceeds. Fig. 4b shows the differences of the XPS spectra of Sr3d on the surface of samples at different reduction stages. Three peaks that representing the different chemical states of metal Sr were used to fitting the spectra here, which is Sr_a in the range of E_B at ~131.4 eV representing Sr^+ in low oxidation state [44]; chemical state of Sr_b (~133.1 eV) relates to the double perovskite crystal phase and Sr_c ascribes to the appearance of mixed oxides $SrCoO_z$, La_2SrO_x, and/or SrO phases with higher binding energy. It can be seen that the contents of three species of Sr are similar on the fresh oxygen carrier, suggesting that the Sr_a and Sr_c are also existed in the double perovskite structure. When the reaction starts, the peak areas of Sr_a and Sr_c decrease drastically to 3.41% and 4.39% at 3 min respectively, while the content of Sr_b increases to 92.2%. The reason for this may be that a better-organized double perovskite structure and more regularly coordinated metals are obtained after the rapid separation of the disordered Fe and Co. Therefore, the species of Sr_b that existed in the double structure is presented more. Then as the reaction proceeds, the peak areas of Sr_b gradually decrease from 6 min to the final 20 min, corresponding to the disappearance of double perovskite phase in structure. The content of Sr_c obviously increases due to the emergence of La_2SrO_x, which is compatible with the XRD results.

The integral XPS spectra of Fe2p at different reduction stages are shown in Fig. 4c. Deconvolution of the peak shows up an asymmetry feature with double-peaked spectrum, accompanying with the satellite peak at E_B of ~718 eV [45]. The peak that positioned at ~710 eV is the characteristic of mixed valence states of Fe^{3+} and Fe^{2+} [46], while the peak at E_B of ~713 eV is corresponding to the chemical state of Fe^{4+} [47]. The emergence of Fe^{4+} is mainly ascribing to the electronic unbalance in the double perovskite structure which is aroused by the substitution of Sr for La. Metals with high valence states and/or more oxygen vacancies are generated to compensate the electronic unbalance. Besides, Fe^{5+} may also exit because that the Fe^{4+} is easily to lose electron to form Fe^{5+} [48]. Therefore, the spectra at lower binding energy here are attributed to Fe^{3+} and Fe^{2+}, while the spectra at higher E_B value are assigned to Fe^{4+} and/or Fe^{5+}. It can be seen from Table 1 that the Fe^{3+} and Fe^{2+} in low valence state are the primary states on the surface of the fresh $La_{1.6}Sr_{0.4}FeCoO_6$. At 3 min, the fraction of Fe^{3+} and Fe^{2+} increase from 56.53% to 65.58%, probably ascribing to the emergence of Fe_2O_3 and the reduction of Fe. Then it shows a tendency to

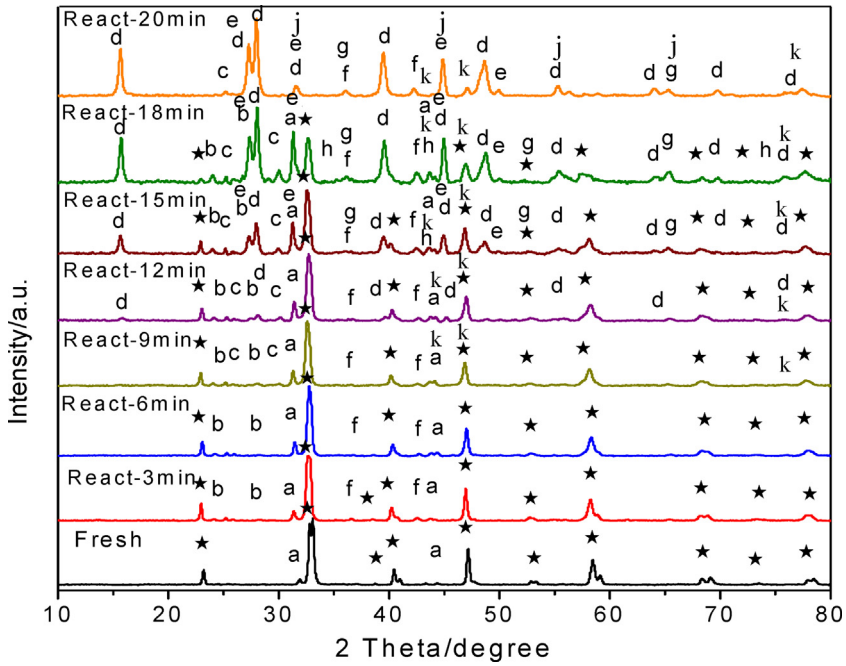

Fig. 3. XRD patterns of $La_{1.6}Sr_{0.4}FeCoO_6$ at different reduction stages.
(⋆-perovskite, a-$SrCoO_z$, b-Fe_2O_3, c-Fe_3O_4, d-La_2SrO_x, f-CoO, e-La_2O_3, g-SrO, h-FeO, j-Fe-Co solid solution, k-Co^0)

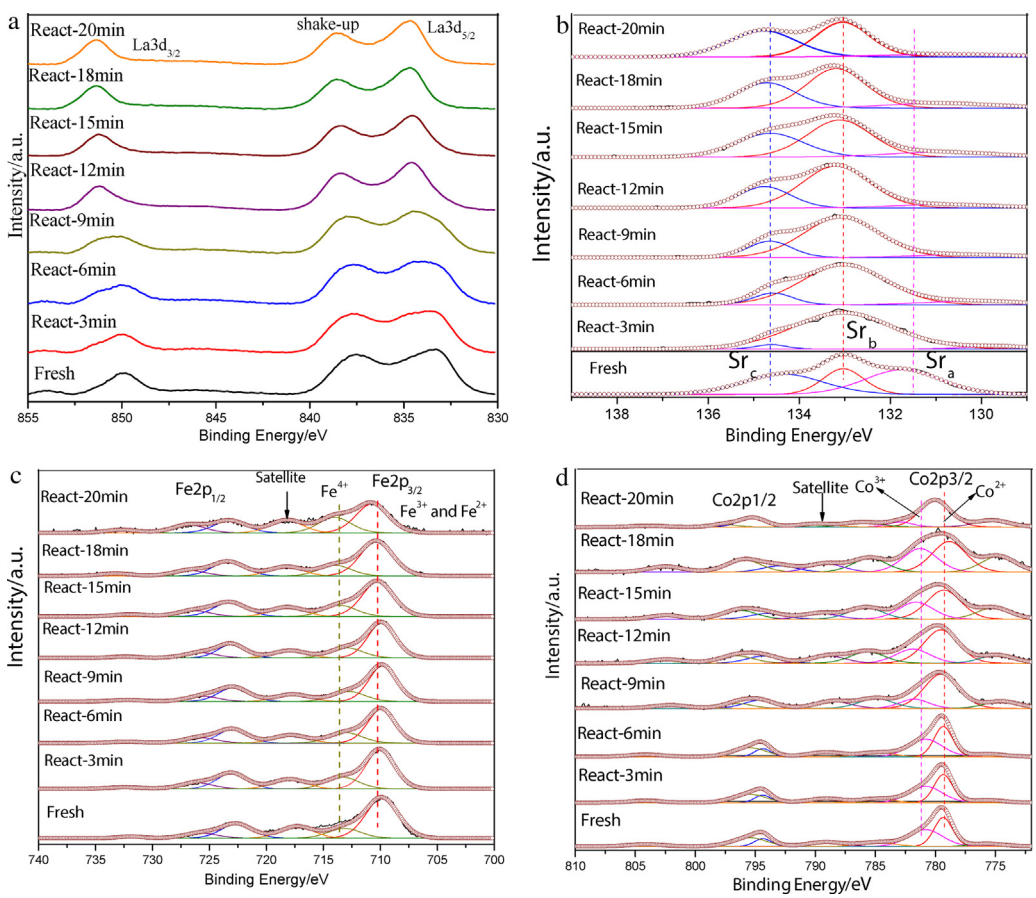

Fig. 4. (1(a)) XPS spectra of La3d in $La_{1.6}Sr_{0.4}FeCoO_6$ at different reduction stages. (2(b)) XPS spectra of Sr3d in $La_{1.6}Sr_{0.4}FeCoO_6$ at different reduction stages. (3(c)) XPS spectra of Fe2p in $La_{1.6}Sr_{0.4}FeCoO_6$ at different reduction stages. (4(d)) XPS spectra of Co2p in $La_{1.6}Sr_{0.4}FeCoO_6$ at different reduction stages.

gently increase as the reduction reaction proceeds, corresponding to the constantly reduction of Fe^{4+} and/or Fe^{5+} to Fe^{3+} and then to Fe^{2+}. Furthermore, the spectrum peak of Fe^0 at binding energy of ~706.7 eV doesn't show up, indicating that the reduction reaction with methane for 20 min is not enough for the deep reduction of Fe^{2+} to Fe^0.

Table 1
Distribution of metal valences from XPS.

Sample	$Sr3d_{5/2}$			$Fe2p_{3/2}$[a]		$Co2p_{1/2}$		
	Peak area (%)			Peak area (%)		Peak area (%)		
	a	b	c	Fe^{3+} and Fe^{2+}	Fe^{4+} and/or Fe^{5+}	Co^{2+}	Co^{3+}	Co^{0}
Frsh	41.14	23.17	35.68	56.53	43.47	60.99	39.01	–
React–3 min	3.41	92.2	4.39	65.58	34.42	61.18	38.82	–
React–6 min	11.35	79.88	8.78	66.91	33.09	62.30	37.70	–
React–9 min	17.71	74.81	7.48	65.56	34.44	63.17	24.67	12.16
React–12 min	25.85	65.80	8.35	67.67	32.33	56.76	30.51	12.73
React–15 min	35.31	52.59	12.10	66.94	33.06	52.98	31.71	15.31
React–18 min	34.44	53.54	12.02	67.42	32.58	51.53	30.68	17.79
React–20 min	46.56	44.50	8.94	69.39	30.61	63.72	19.18	17.10

[a] The ratios of different Fe species are calculated based on the assumption that Fe^{2+}, Fe^{3+}, Fe^{4+} and Fe^{5+} ions were presented in the samples. The spectra at lower binding energy at ~710 eV are attributed to Fe^{3+} and Fe^{2+}. While the spectra at higher E_B value are assigned to Fe^{4+} and/or Fe^{5+}.

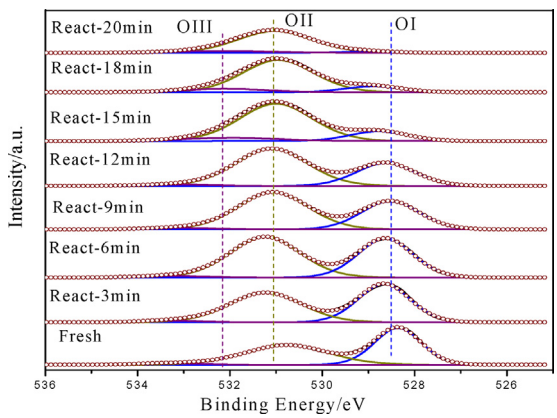

Fig. 5. XPS spectra of O1s on $La_{1.6}Sr_{0.4}FeCoO_6$ at different reduction stages.

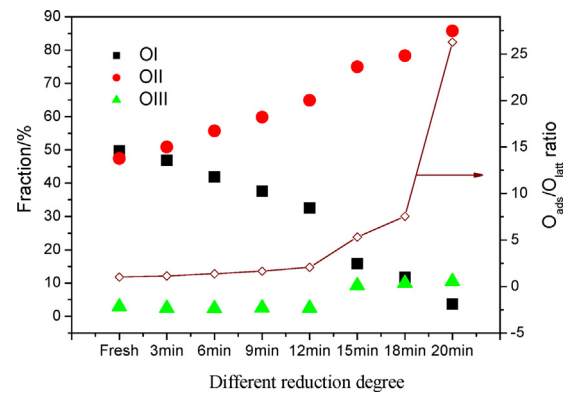

Fig. 6. Distribution of oxygen species on $La_{1.6}Sr_{0.4}FeCoO_6$ at different reduction stages.

Similarly, the asymmetry and broadness of the Co2p peaks showed in Fig. 4d reveal the existence of the mixed valence states of Co ion with Co^{2+} and Co^{3+}. Both Co^{2+} and Co^{3+} are existed on the surface of the fresh $La_{1.6}Sr_{0.4}FeCoO_6$, wherein is dominated by Co^{2+} because that Co^{2+} can be formed easier and more stable than Co^{3+}. As the reaction proceeds, the content of Co^{3+} obviously decreases while the content of Co^{2+} increases, ascribing to the reduction of Co^{3+} to Co^{2+}. After react with CH_4 for 9 min, the species of Co^0 at E_B of ~775 eV obviously appear and increase subsequently, due to the deep reduction of Co^{2+} to Co^0. When the reaction goes to 20 min, the double perovskite structure is collapsed and the fraction of Co^{3+} decreases significantly.

For the O1s spectrum, three oxygen species are observed, which are lattice oxygen (OI) at a low binding energy of 528.4–529.1 eV, chemical adsorbed oxygen (OII) at a binding energy of 530.0–532.0 eV and the hydroxyl and/or carbonate species on the surface (OIII) named physical adsorbed oxygen with binding energy >532.0 eV [49], as shown in Fig. 5.

The distribution of oxygen species derived from the deconvolution of O1s XPS spectra is shown in Fig. 6. It can be seen that the fraction of lattice oxygen (OI) decreases gradually as the reaction proceeds, from the initially 49.67% to the finally 3.67%. While the chemical adsorbed oxygen (OII) increase linearly from 47.45% to 85.79%. The OIII species that represents the physical adsorbed oxygen due to the exposure to atmosphere has no obvious change. Therefore, it can be predicted that the reaction boundary is fixed on the surface of the oxygen carrier. At the beginning of the reaction, the active adsorbed oxygen and lattice oxygen take part in reaction with methane rapidly on the surface of the particles. As the consuming of the oxygen, a concentration gradient of oxygen vacancies is formed on the surface to promote the oxygen transfer from the bulk. When the lattice oxygen transfers from the bulk to surface, most of them are activated to take part in the reduction reaction with methane, meanwhile bits of them are transformed to the chemical adsorbed oxygen with more stable properties through the following pathways: $O_{2(g)} \leftrightarrow O_2{}^{-}{}_{(ads)} \leftrightarrow O_2{}^{2-}{}_{(ads)} \leftrightarrow 2O^{-}{}_{(ads)} \leftrightarrow 2O^{2-}{}_{(ads)} \leftrightarrow 2O^{2-}{}_{(lat)}$ [50], causing the continually decrease of lattice oxygen and the increase of chemical adsorbed oxygen. It also can be seen from Fig. 6 that the O_{ads}/O_{latt} ratio which is proportional to the oxygen defect concentration increases gradually from the beginning of the reaction, which effectively promotes the oxygen diffusivity. But the O_{ads}/O_{latt} ratio increases linearly after 18 min, mainly ascribing to the exhausting of the lattice oxygen.

Table 2 exhibits the surface atomic ratios of the oxygen carrier at different reduction stages that calculated from XPS. Consistent with the previous analysis, the metal La does not take part in the reaction and shows no obvious change of the value. The content of the metal Sr increases in the middle stage of the reaction, ascribing to the better-organized double perovskite structure. And then it shows a tendency to decrease from 12 min. While for the metals in active sites, the contents of Fe and Co show tendency to decrease as the consumption of oxygen, accompanying with the breakage of the Fe—O bond and the Co—O bond in double perovskite structure. By comparison, the migration rate of metal Co is much faster than that of metal Fe, due to the lower bond energy of Co—O which can be broken more easily. Besides, it also can be seen that the ratios of active metals (Fe and Co) to non-active metals (La and Sr) shows a tendency to decrease. It means that the active sites on the surface are gradually decrease while the non-catalytic metals stay on the surface. The decrease of the active metals and the increase of the oxygen on the surface during the reaction reconfirming that the reaction boundary is fixed on the surface of the oxygen carrier. The reaction transportation model for methane reduction over

Table 2
Surface atomic ratio from XPS.

Sample	La3d	Sr3d	Fe2p	Co2p	O1s	(La + Sr)/(Fe + Co)
Frsh	10.27	7.23	3.87	7.93	70.70	1.48
React–3 min	12.42	4.40	7.70	6.00	69.48	1.23
React–6 min	12.49	9.46	6.19	1.63	70.22	2.81
React–9 min	11.42	12.15	5.73	1.05	69.65	3.47
React–12 min	12.28	11.76	5.16	0.63	70.18	4.38
React–15 min	13.08	8.60	4.24	0.85	73.22	4.26
React–18 min	13.38	4.96	3.31	1.26	77.09	4.01
React–20 min	11.08	7.61	1.74	1.37	79.35	6.01

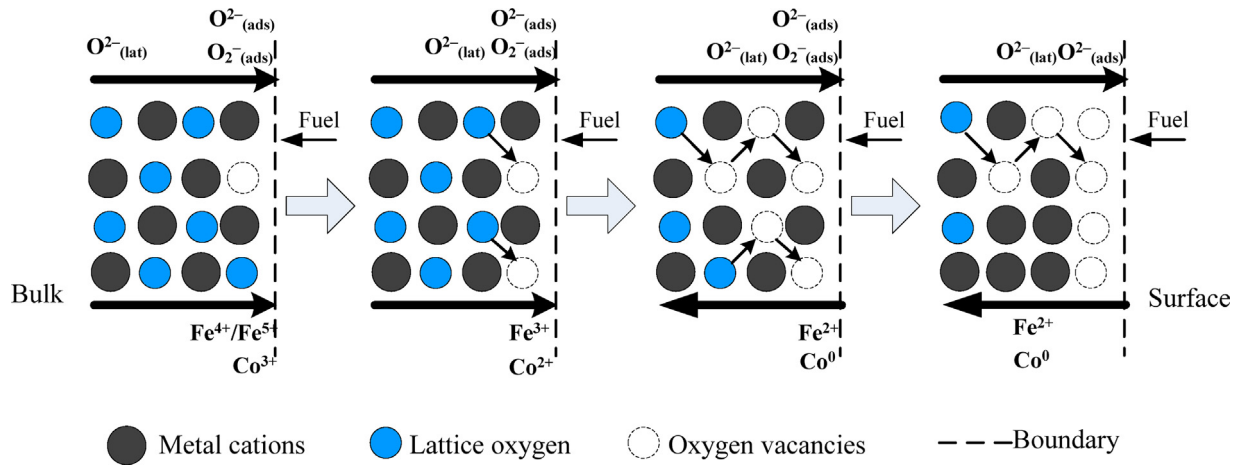

Fig. 7. Reaction transportation model for methane reduction over $La_{1.6}Sr_{0.4}FeCoO_6$.

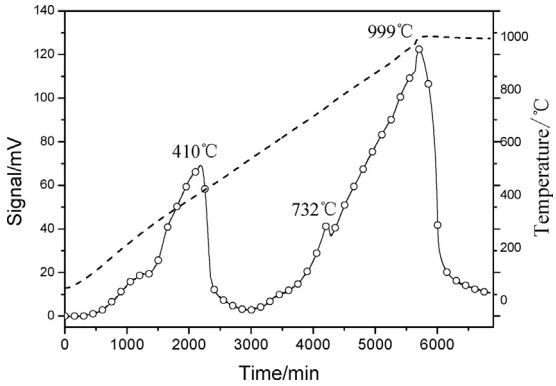

Fig. 8. H_2-TPR profile of $La_{1.6}Sr_{0.4}FeCoO_6$.

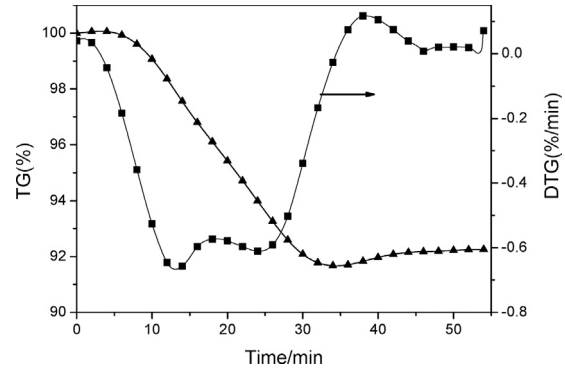

Fig. 9. TG-DTG curves of $La_{1.6}Sr_{0.4}FeCoO_6$.

$La_{1.6}Sr_{0.4}FeCoO_6$ is summarized in Fig. 7. Using the surface of the oxygen carrier particles as reaction boundary, the metal is gradually reduced and migrated inward the bulk, causing the decrease of the active sites for methane dissociation. Meanwhile, the lattice oxygen transfer from the bulk to the boundary to supply oxygen for the reduction reaction.

3.3. H_2-TPR and TG analysis in methane reduction step

Fig. 8 shows the H_2-TPR profile of $La_{1.6}Sr_{0.4}FeCoO_6$ as the function of increasing temperature, which is divided into three parts obviously, ascribing to the three-step reductions. At the beginning of the reaction, hydrogen consumption is gradually increase and gets the maximum value at 410 °C, finally finishes at 587 °C. The appearance of the first reduction peak represents the reduction of adsorbed oxygen which can happen at a relative low temperature, combining with the reduction of metals with high reactivity, such as $Co^{3+} \rightarrow Co^{2+}$ ($Co^{3+} + O_2^- + 2H_2 \rightarrow Co^{2+} + 2H_2O$). After that, a very small reduction peak appears at 732 °C which may due to the quick reduction of Fe^{5+} and/or $Fe^{4+} \rightarrow Fe^{3+}$ ($Fe^{4+}/Fe^{5+} + nO_2^- + nH_2 \rightarrow Fe^{3+} + nH_2O$). Finally, a third reduction peak with very broad peak area emerges and gets the maximum value at 999 °C, ascribing to the bulk reduction of lattice oxygen and the deep reduction of $Co^{2+} \rightarrow Co^0$ ($Co^{2+} + 2O_2^- + 2H_2 \rightarrow Co^0 + 2H_2O$) and $Fe^{3+} \rightarrow Fe^{2+}$ ($Fe^{3+} + O_2^- + H_2 \rightarrow Fe^{2+} + H_2O$). Towards the TG-DTG curves in Fig. 9, three apparent weight loss peaks at 13 min, 24 min and 28 min are also presented respectively in the DTG curve, corresponding to the three reduction stages in H_2-TPR profile. The weight of the sample decreases linearly from the beginning of the reaction to 34 min with the weight loss rate of 8.34 wt.%, suggesting that about 40% of active oxygen is taking part into the reaction. Then the weight of the oxygen carrier increases slightly after 34 min, representing the exhaustion of lattice oxygen and the occurrence of the carbon deposition. At this moment, the deep reduced metals of Fe^{2+} and Co^0 are further attributed to the carbon deposition.

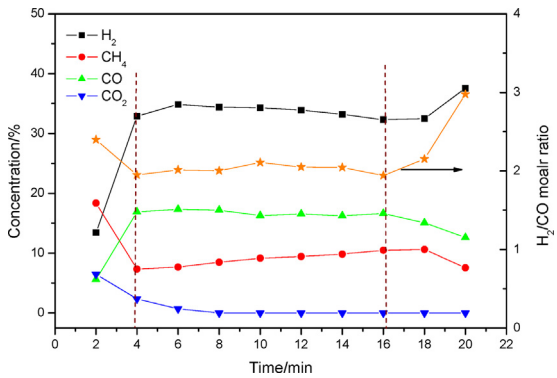

Fig. 10. Gaseous products, H_2/CO molar ratio during the methane reduction.

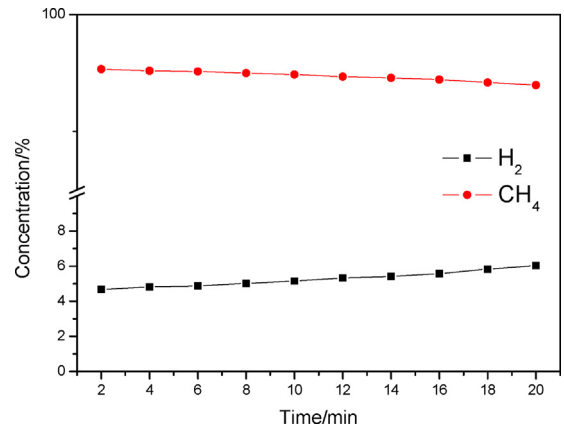

Fig. 11. Blank experiment using quartz sands.

3.4. Reaction mechanism for methane reduction

Generally, the two kinds of oxygen on the DPO exhibit different reaction routes. The surface adsorbed oxygen, named α oxygen with high-activity, is prone to oxidize methane into CO_2 and H_2O. Another kind of lattice oxygen, named β oxygen with moderate activity, is beneficial for the partial oxidation of methane to syngas which is desirable. The gaseous products in the methane reduction stage as well as the corresponding H_2/CO molar ratio are shown in Fig. 10.

The methane reduction process also can be divided into three parts, corresponding to the three reduction stages of metals. (I) At the beginning of the reaction to 2 min, 20% of CH_4 is detected as well as 15% of H_2 and 5% of CO and CO_2 as products. The methane dissociates very fast on the active sites of oxygen carrier and reacts with the large amounts of adsorbed oxygen immediately. The major reactions in this stage may include:

$$CH_4 \rightarrow CH_{x(a)} + (4\text{-}x)H_{(a)} \rightarrow C_{(a)} + 4H_{(a)} \quad (3)$$

$$2H_{(a)} \rightarrow H_{2(g)} \quad (4)$$

$$C_{(a)} + O_{(a)} \rightarrow CO_{(a)} \rightarrow CO_{(g)} \quad (5)$$

$$CH_{x(a)} \text{or} C_{(a)} + O_{(a)} \rightarrow CO_2 + H_2O \quad (6)$$

(II) After 2 min, the concentration of CH_4 decreases sharply and the amounts of CO and H_2 increase correspondingly, and then all of them go to level off after 4 min. Meanwhile, the concentration of CO_2 gradually decreases to the baseline after 8 min. During this stage, the following reactions may be happened:

$$CH_4 \rightarrow C_{(a)} + 4H_{(a)} \quad (7)$$

$$2H_{(a)} \rightarrow H_{2(g)} \quad (8)$$

$$O(\text{bulk}) \rightarrow O(\text{surface}) \rightarrow O_{(a)} \quad (9)$$

$$C_{(a)} + O_{(a)} \rightarrow CO_{(a)} \rightarrow CO_{(g)} \quad (10)$$

$$C_{(a)} + O_{(a)} \rightarrow CO_{2(a)} \rightarrow CO_{2(g)} \quad (11)$$

$$Fe^{4+}/Fe^{5+} \rightarrow Fe^{3+} \rightarrow Fe^{2+} \quad (12)$$

$$Co^{3+} \rightarrow Co^{2+} \rightarrow Co^{0} \quad (13)$$

In this stage, the reduced metals, e.g. Fe^{3+}, Co^{3+} and Co^{2+}, provide the active sites for methane dissociation unceasingly. On the other hand, the oxygen vacancies that induced by oxygen consumption are constantly promoting the migration of lattice oxygen from the bulk to the surface. When the methane dissociation rate gets matching with the lattice oxygen diffusivity, the reaction of R10 is dominatingly happened to produce syngas with H_2/CO molar ratio at 2.0, whereas the reaction R11 tends to stop. During this stage, it also can be seen that the concentration of CH_4 slightly increase while that of H_2 and CO slightly decrease, representing the slowdown of the reaction R7. It may because that the migration of surface active metals inward the bulk causing the decrease of the active sites for methane dissociation. Meanwhile, the constantly consumption of lattice oxygen also decreases the amount of oxygen and consequently decrease the oxygen diffusivity. But they are still existed in a matching state until 16 min. The resistance for carbon deposition is effectively improved by the synergistic effects between multi-metals, and large amounts of syngas are generated. (III) After 18 min, the concentrations of CH_4 and CO decrease quickly, while the concentration of H_2 increase rapidly. The H_2/CO molar ratio increases to much larger than 2.0, ascribing to the methane decomposition. In this stage, the double perovskite structure is collapsed and the lattice oxygen is depleted, following the reactions:

$$CH_4 \rightarrow C_{(a)} + 4H_{(a)} \rightarrow C + 2H_{2(g)} \quad (14)$$

$$Co^{2+} \rightarrow Co^{0} \quad (15)$$

$$Fe^{3+} \rightarrow Fe^{2+} \quad (16)$$

In summary, three reaction stages that happened are distinctly identified, i.e. the total oxidation of methane with active adsorbed oxygen to produce CO_2 and H_2O, the partial oxidation of methane with lattice oxygen to generate CO and H_2, and the methane decomposition to form carbon deposition. Fig. 11 shows the blank experiment results of methane pyrolysis using the quartz sands as bed materials. It can be seen that the concentration of methane has almost no change during the whole reaction, without methane decomposition. That means the methane dissociation is mainly happened on the active sites of the oxygen carrier. Hormilleja et al. [51] produced hydrogen from chemical looping conversion of bioethanol and found that the carbon deposition was mainly formed through the decomposition of hydrocarbon fuel and the Boudouard reaction. But whether the decomposition reaction or the Boudouard reaction, they have very slow reaction speeds if without metal active sites considering from the point of dynamics. Therefore, the existence of metals with high valences such as Fe^{5+} and/or Fe^{4+} combining Co^{3+}, introduced by the substitution of Sr for La in the double perovskite structure, providing abundant active sites for methane dissociation at the beginning of the reaction. Meanwhile, the coexistence of multi-metals of Fe—Co in double perovskite structure and the generation of large amounts of oxygen vacancies due to the imbalance of oxidation states between metal sites, synergistically promoted the oxygen diffusion. If the methane dissociation rate is too fast, while the lattice oxygen cannot immediately to supply, the carbon deposition will be formed. On the contrary, if the lattice oxygen release too fast, the excessively lattice oxygen will transform to the adsorbed oxygen which lead to the total oxidation of methane to generate CO_2 and H_2O or

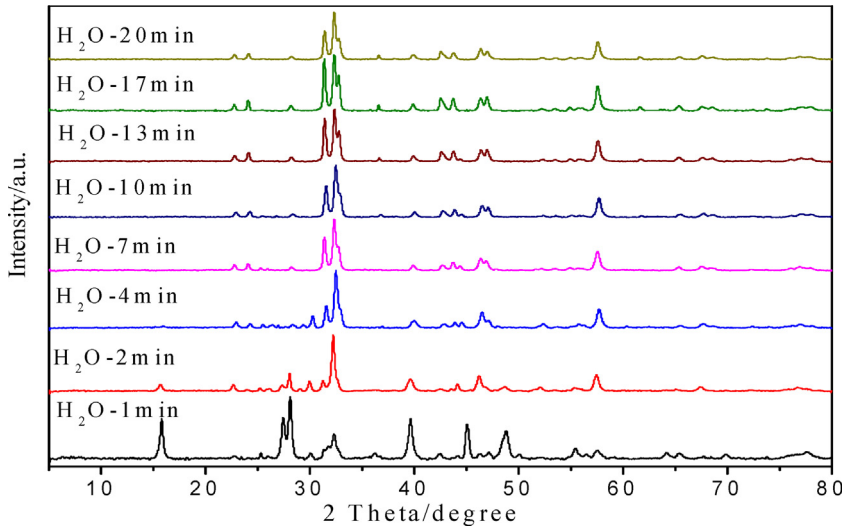

Fig. 12. XRD patterns of oxygen carrier in different oxidation stage.

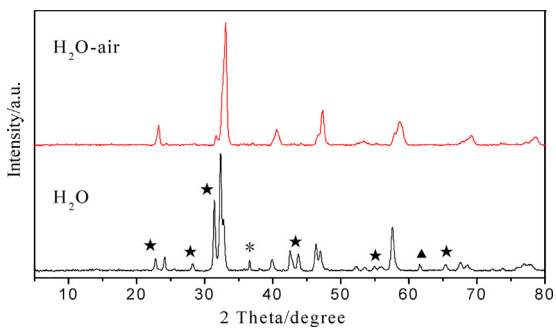

Fig. 13. XRD patterns of regenerated oxygen carrier. (⋆$LaSrFeO_4$, *$CoCo_2O_4$, ▲Fe_2O_3)

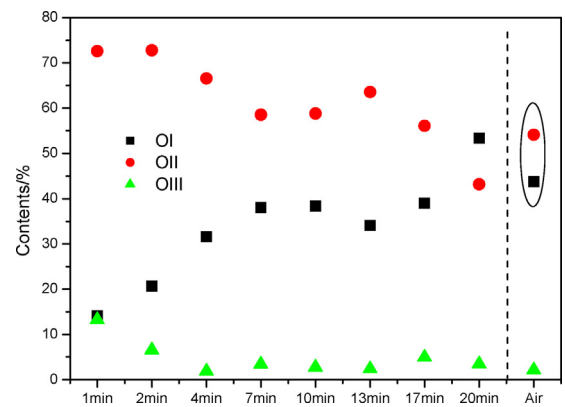

Fig. 14. Distribution of oxygen species on $La_{1.6}Sr_{0.4}FeCoO_6$ at different oxidation stage.

transform to a more stable species to fixed on the reaction boundary. Otsuka et al. [52] proposed the direct reaction mechanism of methane reduction with lattice oxygen by using CeO_2 as oxygen carrier. They regarded the metal active sites and the oxygen vacancies as the most important factors in methane conversion, which is consistent with the results here.

3.5. XRD analysis in steam dissociation step

After reduction, steam is introduced in for the regeneration of the reduced oxygen carrier and simultaneously the steam is dissociated to generate hydrogen. The XRD patterns of oxygen carriers at different oxidation stages are shown in Fig. 12. When the steam dissociation reaction proceeds to 2 min, the characteristic peaks of La_2SrO_x and La_2O_3 are obviously disappeared, suggesting that the metals in A and A' sites are very easy to be regenerated. After that, there is no obvious change for the XRD patterns as the reaction proceeds, except the gradually improvement of crystallinity for the double perovskite structure. Finally, the double perovskite structure still cannot go back to its original state after 20 min of reaction, accompanying with some impurity phases such as $LaSrFeO_4$, $CoCo_2O_4$ and Fe_2O_3 (see Fig. 13). The complexity of the double perovskite structure makes it difficult to form coordination for all the metals. Therefore, further oxidation by air is necessary to be introduced in. It can be seen from Fig. 13 that the impurity phases are thoroughly disappeared and the double perovskite structure is recovered to its original state after air oxidation.

3.6. XPS analysis in steam dissociation step

The oxygen regenerated by steam is investigated by XPS and the distribution of oxygen species at different oxidation stages are shown in Fig. 14. The content of lattice oxygen (OI) increase as the reaction proceeds, while the chemical adsorbed oxygen (OII) shows a tendency to decrease. After reacted with steam for 20 min, the content of lattice oxygen is recovered to 50%, the same as its original state. It means that the lattice oxygen can be totally recovered by steam. However, it's interesting that the content of lattice oxygen decrease after air oxidation and its dominating status is replaced by the chemical adsorbed oxygen. Air has a higher oxidative property, causing more adsorbed oxygen concentrated on the surface of the particles.

3.7. Reaction mechanism for steam dissociation

The gaseous products during the steam dissociation reaction are shown in Fig. 15, which was performed on the reduced sample in a fixed bed reactor. When the steam is introduced in, the H—O bond in H_2O cracks speedy on the active sites of the deep reduced metals of Fe^{2+} and Co^0, combining with the abundant of oxygen vacancies. The oxygen vacancies attract the O atom to supply the vacancies immediately, meanwhile the two H atoms generated from the breaking of H—O bond combine together to form H_2. It can be seen that the hydrogen generation process is very fast, getting the max-

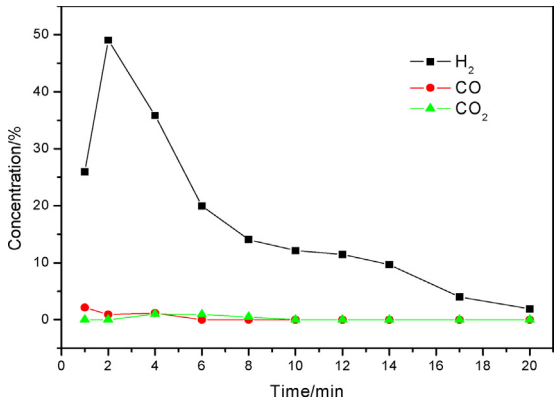

Fig. 15. Gaseous products during the steam dissociation.

imum value of hydrogen concentration at 3 min. Moreover, a small amount of CO_2 is also detected at the original stage due to the carbon deposition in the reduction stage. Then some of CO appears as the decrease of CO_2. According to these, the reactions happened in this stage may include:

$$3FeO + H_2O \rightarrow Fe_3O_4 + H_2 \quad (18)$$

$$2Fe_3O_4 + H_2O \rightarrow 3Fe_2O_3 + H_2 \quad (19)$$

$$Co + H_2O \rightarrow CoO + H_2 \quad (20)$$

$$La_{x1}Sr_{x2}Fe_{x3}Co_{x4}O_{6-\delta1-\delta2} + H_2O \rightarrow La_{1.6}Sr_{0.4}FeCoO_{6-\delta1} \quad (21)$$

$$C + 2H_2O \rightarrow CO_2 + 2H_2 \quad (22)$$

$$C + CO_2 \rightarrow 2CO \quad (23)$$

As the reaction proceeds to go on, the capacity for steam splitting is gradually recede, following by the supplement of oxygen vacancies and the recharge of the metal valences. At this moment, most of the lattice oxygen is recovered and the hydrogen fraction gradually decreases to 1.9% at 20 min. Based on the discussions above, the reaction mechanism model for CL-SMR over $La_{1.6}Sr_{0.4}FeCoO_6$ is proposed as shown in Fig. 16. The reduction of metals into low valence states by methane is the material basis for steam splitting, which can provide active sites for the cleavage of H—O bond. But at the same time, the deep reduced metals are also the catalysts for the formation of carbon deposition when the lattice oxygen is depleted. Therefore, how to realize the synchronization of methane dissociation, metals reduction and the lattice oxygen diffusion is crucial. The design of efficient oxygen carriers for CL-SMR must consider the balance among the concentration of active sites for recants activation, the oxygen diffusivity and the available oxygen store capacity, consequently to obtain the target product more accurately. Such findings warrant further investigations of chemical looping combustion (CLC) by adjusting the solid circulating rate to realize the total oxidation of carbon fuel, consequently to achieve carbon capture and storage (CCS) just through condensation of H_2O without excess energy consumption. The thermo stability at high temperature also made it very attractive for the purpose of chemical looping in real applications.

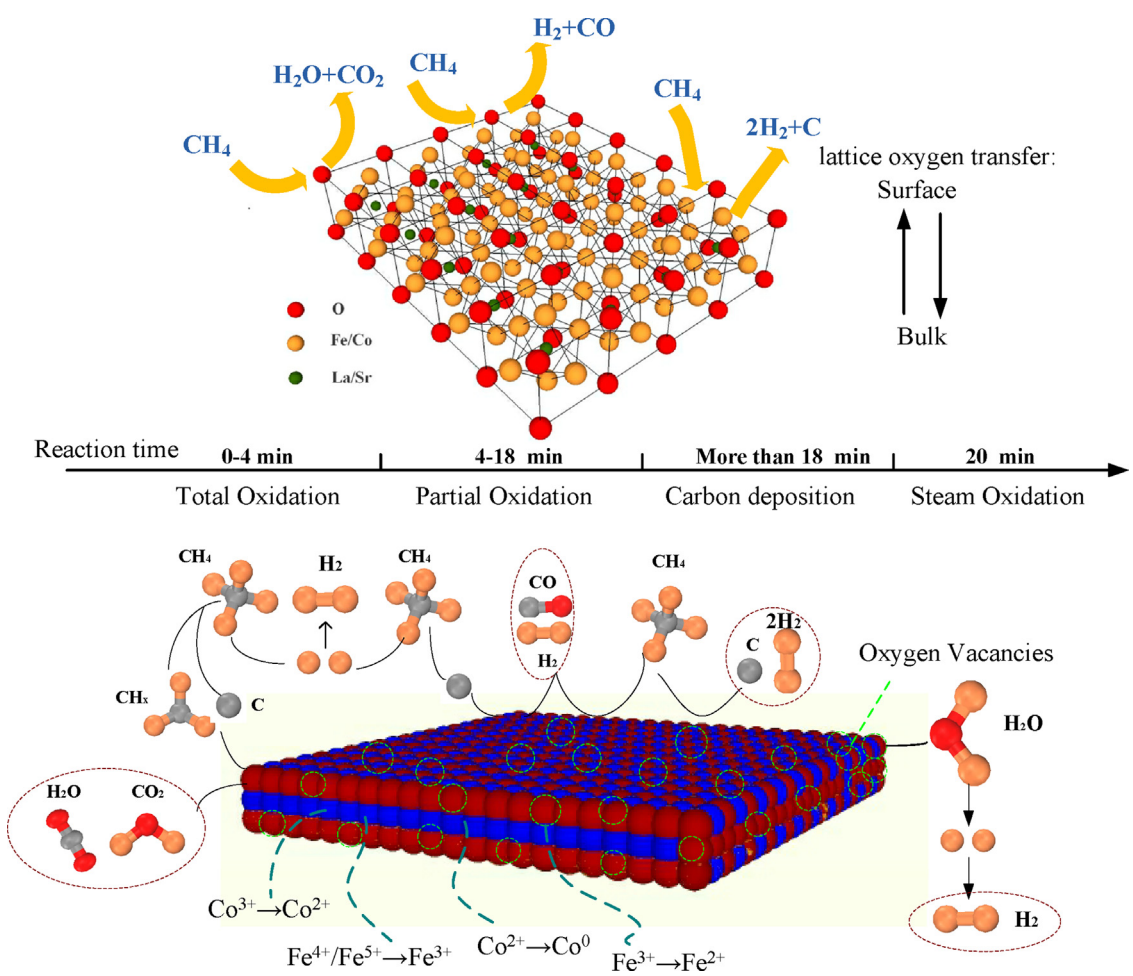

Fig. 16. Reaction mechanism model for CL-SMR over $La_{1.6}Sr_{0.4}FeCoO_6$.

4. Conclusions

Double perovskite-type oxide $La_{1.6}Sr_{0.4}FeCoO_6$ was prepared by micro-emulsion method and used as oxygen carrier for CL-SMR to co-produce syngas and hydrogen. The substitution of Sr for La induces the formation of metals with high valence states such as Fe^{5+}, Fe^{4+} and Co^{3+} in B and B' sites, which provide active sites for methane dissociation. Meanwhile, the coexistence of multi-metals of Fe-Co in double perovskite structure promotes the oxygen diffusion synergistically by inducing abundant oxygen vacancies. The reducibility, oxygen mobility, and steam splitting reactivity are effectively enhanced over $La_{1.6}Sr_{0.4}FeCoO_6$.

In the process of methane reduction, three reaction stages are distinctly identified, i.e. the total oxidation of methane with active adsorbed oxygen to produce CO_2 and H_2O, the partial oxidation of methane with lattice oxygen to generate CO and H_2, and the methane decomposition to form carbon deposition. The decrease of the active metals and the increase of the oxygen on the surface during the reaction demonstrate that the reaction boundary is fixed on the surface of the oxygen carrier particle. During the reduction stage, lattice oxygen transfers from the bulk to the boundary to take part in the methane reduction reaction, meanwhile bits of them are transformed to the chemical adsorbed oxygen with more stable properties. A large number of syngas is generated due to the concordant of methane dissociation with the lattice oxygen diffusion, and the resistant to coke formation is enhanced effectively. In the process of steam dissociation, the deep reduced metals combining with abundant oxygen vacancies provide enough active sites for the breakage of H—O bond of steam. The oxygen vacancies can be supplied immediately by the O atom derived from H_2O. Meanwhile, the two H atoms generated from the bond breaking of H—O combine together to form amounts of H_2. The findings provide a potential way to develop more active oxygen carrier for CL-SMR, by comprehensively considering the methane dissociation and the lattice oxygen diffusion.

Acknowledgments

The financial support of National Key Research and Development Program of China (2016YFB0901401) is gratefully acknowledged. This work was also supported by the National Natural Science Foundation of China (51406208, 51406214). We also thank the support of Science & Technology Research Project of Guangdong Province (2017A020216009, 2015A010106009).

References

[1] M. Prettre, C. Eichner, M. Perrin, Trans. J. Faraday Soc. 43 (1946) 335–339.
[2] G. Pantaleo, V. La Parola, F. Deganello, R.K. Singha, R. Bal, A.M. Venezia, Appl. Catal. B: Environ. 189 (2016) 233–241.
[3] Z. Boukha, C. Jiménez-González, M. Gil-Calvo, B. de Rivas, J.R. González-Velasco, J.I. Gutiérrez-Ortiz, R. López-Fonseca, Appl. Catal. B: Environ. 199 (2016) 372–383.
[4] M.C. Tang, L. Xu, M.H. Fan, Appl. Energy 151 (2015) 143–156.
[5] V. Kyriakou, I. Garagounis, A. Vourros, E. Vasileiou, A. Manerbino, W.G. Coors, M. Stoukides, Appl. Catal. B: Environ. 186 (2016) 1–9.
[6] C. Zhao, Z. Zhou, Z. Cheng, X. Fang, Appl. Catal. B: Environ. 196 (2016) 16–26.
[7] X. Zhu, Y.G. Wei, H. Wang, K.Z. Li, Int. J. Hydrogen Energy 38 (2013) 4492–4501.
[8] A. Steinfeld, P. Kuhn, J. Karni, Energy 18 (1993) 239–249.
[9] A. Steinfeld, A. Frey, P. Kuhn, D. Wuillemin, Int. J. Hydrogen Energy 20 (1995) 793–804.
[10] T. Kodama, T. Shimizu, T. Satoh, K.-I. Shimizu, Energy 28 (11) (2003) 1055–1068.
[11] K.Z. Li, H. Wang, Y.G. Wei, D.X. Yan, Appl. Catal. B: Environ. 197 (2010) 361–372.
[12] K.Z. Li, H. Wang, Y.G. Wei, D.X. Yan, J. Chem. Eng. 156 (2010) 512–518.
[13] S.G. Kang, R.S. Sung, D.K. Sang, Int. J. Hydrogen Energy 33 (2008) 5986–5995.
[14] T. Kodama, T. Shimizu, T. Satoh, M. Nakata, K.I. Shimizu, Sol. Energy 73 (2002) 363–374.
[15] M. Rydén, H. Leion, T. Mattisson, A. Lyngfelt, Appl. Energy 113 (2014) 1924–1932.
[16] O. Mihai, D. Chen, A. Holmen, Ind. Eng. Chem. Res. 50 (2011) 2613–2621.
[17] K. Zhao, F. He, Z. Huang, A.Q. Zheng, H.B. Li, Z.L. Zhao, Int. J. Hydrogen Energy 39 (2014) 3243–3252.
[18] X.P. Dai, J. Cheng, Z.Z. Li, M.Z. Liu, Y.D. Ma, X. Zhang, Chem. Eng. Sci. 153 (2016) 236–245.
[19] X.P. Dai, J. Li, J.T. Fan, W.S. Wei, J. Xu, Ind. Eng. Chem. Res. 51 (2012) 11072–11082.
[20] O. Mihai, D. Chen, A. Holmen, J. Catal. 293 (2012) 175–185.
[21] Y.E. Zheng, K.Z. Li, H. Wang, D. Tian, Y.H. Wang, X. Zhu, Y.G. Wei, M. Zheng, Y.M. Luo, Appl. Catal. B: Environ. 202 (2017) 51–63.
[22] F. He, X.A. Li, K. Zhao, Z. Huang, G.Q. Wei, H.B. Li, Fuel 108 (2013) 465–473.
[23] D.D. Taylor, N.J. Schreiber, B.D. Levitas, W.Q. Xu, P.S. Whitfield, E.E. Rodrigues, Chem. Mater. 28 (2016) 3951–3960.
[24] A. Evdou, V. Zaspalis, L. Nalbandian, Fuel 89 (2010) 1265–1273.
[25] A. Shafiefarhood, N. Galinsky, Y. Huang, Y.G. Chen, F.X. Li, Chem. Catal. Chem. 6 (2014) 790–799.
[26] L.M. Neal, A. Shafiefarhood, F.X. Li, ACS Catal. 4 (2014) 3560–3569.
[27] N. Galinsky, M. Sendi, L. Bowers, F.X. Li, Appl. Energy 174 (2016) 80–87.
[28] L. Nalbandian, A. Evdou, V. Zaspalis, Int. J. Hydrogen Energy 36 (2011) 6657–6670.
[29] K. Zhao, F. He, Z. Huang, G.Q. Wei, A.Q. Zheng, H.B. Li, Z.L. Zhao, Appl. Energy 168 (2016) 193–203.
[30] P. Vibhav, V. Vivek, R.P. Aloysius, G.L. Bhalla, V.P.S. Awana, H. Kishan, J. Magn. Magn. Mater. 321 (2009) 2239–2244.
[31] H.M. Chen, X.X. Xu, Appl. Catal. B: Environ. 206 (2017) 35–43.
[32] M.M. Saad, J. Alloys Compd. 587 (2014) 652–658.
[33] Z.H. Du, H.L. Zhao, S. Yi, Q. Xia, Y. Gong, Y. Zhang, X. Cheng, Y. Li, L. Gu, K. Swierczek, ACS Nano 10 (2016) 8660–8669.
[34] H. Falcón, J.A. Barbero, G. Araujo, M.T. Casaisc, M.J. Martínez-Lopec, J.A. Alonsoc, J.L.G. Fierro, Appl. Catal. B 53 (2004) 37–45.
[35] C. Li, W.D. Wang, C.Y. Xu, Y.X. Liu, B. He, C.S. Chen, J. Nat. Gas Chem. 20 (2011) 345–349.
[36] C. Li, W.D. Wang, N. Zhao, Y.X. Liu, B. He, F.C. Hu, C.S. Chen, Appl. Catal. B: Environ. 102 (1–2) (2011) 78–84.
[37] R.S. Hu, R.R. Ding, J. Chen, J.N. Hu, Y.L. Zhang, Catal. Commun. 21 (2012) 38–41.
[38] J.J. Li, R.S. Hu, J.G. Zhang, W.W. Meng, Y.F. Du, Y.F. Si, Z. Zhang, Fuel 178 (2016) 148–154.
[39] R.S. Hu, Y.Q. Bai, H.Y. Du, H.M. Zhang, Y.F. Du, J.G. Zhang, Q.H. Zhou, J. Rare Earths 33 (2015) 1284–1292.
[40] P.V. Tuza, M.M.V.M. Souza, Catal. Lett. 146 (2016) 47–53.
[41] K. Zhao, L.W. Li, A.Q. Zheng, Z. Huang, F. He, Y. Shen, G.Q. Wei, H.B. Li, Z.L. Zhao, Appl. Energy 197 (2017) 303–404.
[42] K. Zhao, Y. Shen, F. He, Z. Huang, G.Q. Wei, A.Q. Zheng, H.B. Li, Z.L. Zhao, Appl. Energy 168 (2016) 193–203.
[43] J.K. Murthy, K.D. Chandrasekhar, H. Wu, H. Yang, J. Lin, A. Venimadhav, J. Phys: Condens. Matter 28 (2016) 1–11.
[44] V.N. Stathopoulos, V.C. Belessi, T.V. Bakas, S.G. Neophytides, C.N. Costa, P.J. Pomonis, A.M. Efstathiou, Appl. Catal. B: Environ. 93 (2009) 1–11.
[45] A.E. Bocquet, A. Fujimori, T. Mizokawa, T. Saitoh, H. Namatame, S. Suga, N. Kimizuka, Y. Takeda, M. Takano, Phys. Rev. B 45 (1992) 1561–1570.
[46] T. Yamashita, P. Hayes, Appl. Surf. Sci. 254 (2008) 2441–2449.
[47] H.M. Widatallah, A.D. Al-Rawas, C. Johnson, S.H. Al-Harthi, A.M. Gismelseed, E.A. Moore, S.J. Stewart, J. Nanosci. Nanotechnol. 9 (2009) 2510–2517.
[48] A.D. Al-Rawas, H.M. Widatallah, S.H. Al-Harthi, C. Johnson, A.M. Gismelseed, M.E. Elzain, A.A. Yousif, Mater. Res. Bull. 65 (2015) 142–148.
[49] K.Z. Li, H. Wang, Y.G. Wei, D.X. Yan, Int. J. Hydrogen Energy 36 (2011) 3471–3482.
[50] Y.G. Wei, H. Wang, K.Z. Li, X. Zhu, Y.P. Du, J. Rare Earths 28 (2010) 560–565.
[51] E. Hormilleja, P. Durán, J. Plou, J. Herguido, J.A. Peña, Int. J. Hydrogen Energy 39 (2014) 5267–5273.
[52] K. Otsuka, W. Ye, E. Sunada, I. Yamanaka, J. Catal. 175 (1998) 152–160.